PAPER

An atom probe tomography and inventory calculation examination of second phase precipitates in neutron irradiated single crystal tungsten

An atom probe tomography and inventory calculation examination of second phase precipitates in neutron irradiated single crystal tungsten

Philip D. Edmondson[1] , **Baptiste Gault**[2,3] **and Mark R Gilbert**[4]

[1] Materials Science & Technology Division, Oak Ridge National Laboratory, Oak Ridge, TN 37831 United States of America
[2] Department of Microstructure Physics and Alloy Design, Max-Planck-Institut für Eisenforschung GmbH, Max-Planck-Straße, Düsseldorf 40237, Germany
[3] Department of Materials, Royal School of Mines, Imperial College London, Exhibition Road, London, SW7 2AZ, United Kingdom of Great Britain and Northern Ireland
[4] CCFE, UK Atomic Energy Authority, Culham Science Centre, Abingdon, OX14 3DB, United Kingdom of Great Britain and Northern Ireland

E-mail: edmondsonpd@ornl.gov

Abstract
Tungsten is the prime candidate material for the plasma facing divertor system and first wall armor of future nuclear fusion reactors. However, the understanding of the microstructural and chemical evolution of pure tungsten under neutron irradiation is relatively unknown, in part due to a lack of experimental data on this topic. Here, single crystal tungsten has been irradiated in the High Flux Isotope Reactor (HFIR) at Oak Ridge National Laboratory at a nominal temperature of 700–800 °C to damage levels of 0.1 and 1.8 displacements per atom (dpa). Inventory calculations of the neutron irradiation experiments have been used to track isotope generation and decay to inform atom probe tomography (APT) results in the determination of the transmutation-induced precipitate compositions. Furthermore, APT crystallography has been used to show the relationship between precipitates and matrix. The composition of the precipitates is shown to progress towards that of the σ-phase at the highest dose studied, with those precipitates lying along crystallographic planes similar to those of displacement-induced dislocations. This work also sets the framework for APT studies of materials that contain isotopic ratios far from those observed in the natural state.

Keywords: tungsten, atom probe tomography, inventory calculations, precipitation, fusion, neutron irradiation

(Some figures may appear in colour only in the online journal)

1. Introduction

The divertor of a nuclear fusion power reactor is a key component in which the exhaust gases are directed to ensure continued optimal plasma performance. Under normal operating conditions, the divertor material is expected to face extremely harsh environments including intense neutron irradiation fields, high temperatures, direct impacts from the plasma, etc. For these reasons, the material selection is particularly challenging. One candidate material is tungsten due to its low sputtering rate, high thermal conductivity, and low transmutation rate [1–3]. For these reasons, tungsten is also one of the leading candidates for the armor lining of the first wall that covers the tritium breeding zones of fusion reactors; here the neutron intensity is even higher although the temperatures and plasma interactions will be lower. However, the use of tungsten is made problematic by its inherent brittleness and high brittle-to-ductile transition temperature (DBTT) of ~ 400–$500\,^\circ$C that only becomes worse under irradiation due to a combination of defect production and evolution, and the formation of second phase precipitates composed of transmutation products (primarily, Re and Os).

Much research has been performed on the nature of dislocation loops formed under ion and neutron irradiation in tungsten and tungsten model alloys [4–7]. Broadly it is found that dislocations with Burgers vector, $\mathbf{b} = \frac{1}{2}\langle 111 \rangle$ and $\langle 100 \rangle$ are produced, regardless of the starting composition, for irradiation temperatures in the range 300–750 $^\circ$C; however, it has been observed that the distribution of vacancy- and interstitial-type dislocations and the ratios of the Burgers vectors of such dislocations is correlated with the initial composition of the material [5, 6].

Considerably less effort has focused on the characterisation of precipitates in irradiated tungsten, with recent efforts by Xu *et al* [8, 9] on model W-based alloys revealing that the clusters formed above and below the vacancy mobility temperature in W-2Re, W-1Re-1Os, and W-2Re-1Ta (composition in at.%) when self-ion irradiated up to 33 displacements per atom (dpa). Transmission electron microscopy (TEM) investigations [10] of neutron-irradiated W-based alloys in the JOYO reactor at temperatures between 400 and 750 $^\circ$C also revealed the presence of needle-like shaped precipitates, however due to the limitations of the imaging technique used, it was not possible to accurately determine the composition and specific structure and crystallographic relationships with the surrounding matrix.

Whilst the use of ion irradiation studies of the types described above are very useful in performing fundamental, single variable studies to enable the elucidation of mechanistic understandings of how displacement events caused by irradiation results in microstructural evolution, they do not fully capture the nucleation, evolution and growth of the second phase precipitates in the highly dynamic (chemically and structurally) environment of a power reactor. As such it is necessary to undertake neutron-irradiation studies to understand how these complexities operate in a holistic manner during service.

In order to understand the precipitation induced degradation of the properties of tungsten, particularly as it pertains to tungsten's use in nuclear fusion applications, it is necessary to understand the precipitate nucleation, growth, and local chemistry at an atomistic level. By achieving this, and developing atomistic and mechanistic models of property degradation based on this data, it will allow for the design and development of new materials and/or mitigation strategies that will better enable the realisation of nuclear fusion power reactors. To this aim, we have performed a combinatorial study of neutron irradiated single crystal tungsten through the application of inventory-calculation-informed atom-probe-tomography (APT) to track the evolution of the precipitates as the constituent matrix atoms transmute and cluster/precipitate into non-equilibrium secondary phases that are detrimental to the physical properties. The insights gained through this study will enable a deeper understanding of the physical mechanisms driving precipitate formation under *in operando* conditions.

2. Materials & methods

2.1. Materials & irradiations

The material used for this work was a single crystal tungsten provided by Goodfellow Corporation and the bulk composition is given in table 1. The crystal growth direction was $\langle 110 \rangle$. Tensile bars of standard SS-J2 geometry were cut along this zone axis, but the surface normal was not measured at the time of sample fabrication. The tensile bars were then loaded into irradiation vehicles known as '*rabbits*' designed to have a nominal irradiation temperature of 650 $^\circ$C , a temperature that is above the vacancy mobility limit for tungsten. [8, 9]

Irradiations were performed using Oak Ridge National Laboratory's High Flux Isotope Reactor (HFIR) using the Hydraulic Tube Facility (HTF). Use of the HTF allows for the irradiation rabbits to be inserted into the reactor for non-integer cycle timescales (a typical HFIR irradiation cycle is 21 days). In doing this, both low ($<$1 dpa) and higher ($>$1 dpa) fluence irradiations may be conducted.

Two samples have been examined in this study—one low dose, and one high dose specimen. The irradiation conditions are given in table 2 in which the actual irradiation temperature is given following analysis of passive SiC temperature monitors included in the irradiation rabbit [11]. Meanwhile, the damage, measured in displacements per atom (dpa), is calculated based on a conversion for tungsten irradiated in the HTF of HFIR of 0.195 dpa for a neutron fluence of 1.0×10^{25} n·m^{-2}, specific to these irradiation conditions, i.e. place in reactor and reactor type.

Following removal from HFIR and a cooling period of up to 150 days, the rabbits were transferred to the hot cell facilities at ORNL for tensile testing. Following tensile testing, one half of the broken tensile specimens were transferred to ORNL's Low Activation Materials Development and Analysis

Table 1. Composition of the single crystal tungsten sample used in this study.

	W	O	N	C	S	H	Cu
wt.%	Bal.	0.001	<0.001	0.001	<0.000 5	0.000 3	<0.005
at.%	Bal.	0.011	<0.013	0.015	<0.003	0.055	<0.014

Table 2. Irradiation conditions for the two specimens examined in this work. The target temperature for irradiation was 650 °C .

Sample ID	Irradiation Temperature (°C)	Fluence (10^{25} n.m^{-2})	Experimental time*	dpa	
1W51	690	0.54	160 hours	0.1	'low dose'
1W19	770	9.00	185 days	1.8	'high dose'

*Total time including all irradiation cycles and periods of cooling up to end of last cycle

(LAMDA) Laboratory for microstructural analysis and characterisation.

2.2. Inventory calculations

Inventory calculations were performed using the inventory code FISPACT-II [12] and TENDL-2017 [13] nuclear data library. FISPACT-II has been developed to perform calculations of the activation of materials bombarded with energetic neutrons (or charged particles) in nuclear environments, and thereafter to trace the activation-decay during post-irradiation cooling. It achieves this through detailed evolution of the nuclide/isotope inventory (i.e. the material composition) as a function of time using numerical solutions to coupled differential equations describing the change in composition (transmutation) of each nuclide according to their reaction rates and decay half-life—both obtained from extensive nuclear data libraries (i.e. TENDL-2017 here).

Important input parameters for FISPACT-II are the neutron flux, neutron-energy spectrum, the initial starting material isotopic distribution, and irradiation and decay history. For this work, the neutron flux used for the calculations was 4.35×10^{15} neutrons.cm^{-2}.s^{-1} and the neutron-energy spectrum corresponded to the irradiation position of the samples in HFIR (evaluated using neutron transport simulations). The neutron spectrum in the HTF region is given in figure 1. The material was assumed to be pure tungsten with bulk natural abundance: 0.12 at.% ^{180}W, 26.498 at.% ^{182}W, 14.314 at.% ^{183}W, 30.642 at.% ^{184}W, and 28.426 at.% ^{186}W.

In order to produce the most accurate data possible, the FISPACT-II simulations were set up to mimic the HFIR irradiations and the cooling exactly. This was achieved by modeling the irradiation cycles faithfully, i.e. during the high fluence irradiation which covered multiple cycles, the material was allowed to decay-cool in between cycles, and also in between the time from removal from the HFIR up until the date of data collection in the atom probe. In the short-term (particularly between cycles), correct modelling of the decay-cooling allows the sample to evolve towards the dominant stable nuclides of Re and Os produced in neutron-irradiated W.

2.3. Atom probe tomography analysis

Specimens to be characterised using atom probe tomography (APT) were prepared from the undeformed head region of the broken (tested) tensile test specimen using a focused ion beam technique [14]. Data was acquired on a CAMECA Instruments LEAP 4000X HR local electrode atom probe located at the Center for Nanophase Materials Science (CNMS) at ORNL. All data was collected using pulsed laser mode, with a base temperature of 50 K, pulse frequency of 10 kHz, pulse energy of 50 pJ, and an evaporation rate of 0.005 ions per pulse. Reconstructions of the obtained data was performed using CAMECA's Integrated Visualization and Analysis Software, IVAS, version 3.6.12 software, using a reverse point projection method based on atom probe crystallography. [15]

Precipitates were highlighted using a composition isosurface based on the Re and Os peaks assigned in the mass-to-charge-state spectrum, and the atoms contained within that composition isosurface were extracted using IVAS in a *.pos* file format. This file format contains the 3-dimensional positions of each individual ion (as *x, y,* and *z*), and the mass-to-charge-state ratio. Compositions of the matrix and the exported composition isosurfaces were determined from the *.pos* file using a peak deconvolution method [16] using the isotopic abundances given by the inventory calculations (as described above) rather than the natural isotopic abundances. The manual decomposition of the non-natural abundance peaks followed the equation given in equation (1) where A_i is the actual total number of counts for an unknown ion, i; M_j is the measured counts of the ranged ion j; f_{ij} is the isotopic abundance that isotype i has in the range j; and α_{ij} is the unknown fractions of the ions in range j that are of type i [16].

$$f_{ij}A_i = \alpha_{ij}M_j \qquad (1)$$

3. Results and discussion

The reconstructed atom maps for both the low dose (0.1 dpa) and high dose (1.8 dpa) are shown in figure 2. In both cases, isocomposition surfaces are used to reveal the presence of
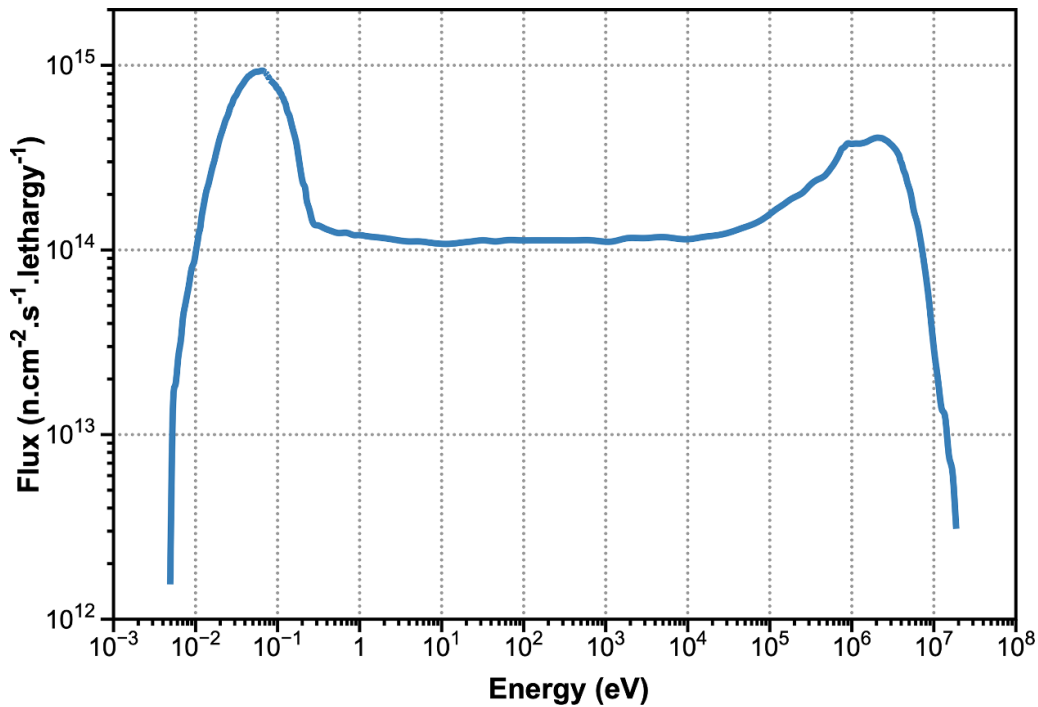
Figure 1. HFIR neutron energy spectrum at the flux trap region where the specimens characterised in this work were irradiated.

nanoscale clusters/precipitates in the bulk material. For the low dose specimen shown in figure 2(*a*), a 1 at.% ReOs iso-composition surface reveals the presence of nanoscale spherical clusters randomly distributed throughout the matrix; the higher dose specimen (figure 2(*b*), 12 at.% ReOs) reveals a complex network of rod- and ribbon-like precipitates.

A reduced section taken from the background corrected, mass-to-charge-state spectrum for the high dose specimen is shown in figure 3. Here, the experimentally obtained mass-to-charge-state data is shown as a green line. Overlaid on the graph are the natural abundance ratios for the different isotopes of W, Re, and Os for a bulk composition as determined using the peak decomposition algorithm native to IVAS. The open points in figure 3 represent the values for the natural abundances for the bulk low dose composition, whereas the filled points represent the natural abundances for the bulk high dose composition. It is evident that the use of natural abundances is unsuitable for accurate compositional analysis of the second phase precipitates. If composition determination based on the natural abundances was a good match to the experimental data, then the peaks of the spectrum and the natural abundance data points would overlap. The considerable variance between the experimental data and natural abundances clearly demonstrates that the use of natural abundances for the determination of both bulk and precipitate compositions is incorrect, as to be expected. It should be noted explicitly here that due to the expected transmutation of the W isotopes into other elemental species having the same isotopic ratio, there is considerable isobaric overlap for the isotopes of different elements having the same mass-to-charge-state ratio thereby making deconvolution of the composition impossible through the use of natural abundance ratios. The use of natural

abundances to determine cluster/precipitate compositions will lead to incorrect assumptions on the phases, thereby providing invalid data for the development of models on how precipitates form and evolve under reactor-like conditions.

3.1. Determination of bulk and precipitate compositions

As has just been shown, the use of natural abundances to determine the bulk and precipitate compositions in neutron-irradiated tungsten is inaccurate due to the transmutation of the starting material. This is even more evident in reactor cores that have a significant neutron thermal energy component such as that in the HFIR [17] that results in significant transmutation in which Re and Os will be rapidly produced. To correct for the non-natural abundances of the matrix elements, detailed inventory calculations were performed in which more than 100 separate isotopes were tracked from the start of the irradiation experiment up to the date of experimental data collection, the simplified results of which are shown in figure 4. In these graphs only W, Re, and Os are shown for clarity as these are the primary elements remaining in the material post-irradiation. The final compositions from the FISPACT-II simulations are also give in table 3 for the primary elements of interest—Re and Os. Impurities including O, N, and C were also observed at the same levels as given in table 1, along with some minor transmutation products, e.g. Ta, comprising a total elemental composition excluding W, Re, and Os of 0.16 at.%, i.e. 99.84 at.% of the elemental composition is W, Re, and Os.

Using the predicted isotopic ratios determined from the inventory calculations, equation (1) was used to deconvolve the peaks in the mass-to-charge-state spectrum and derive bulk and individual precipitate compositions, the results of which
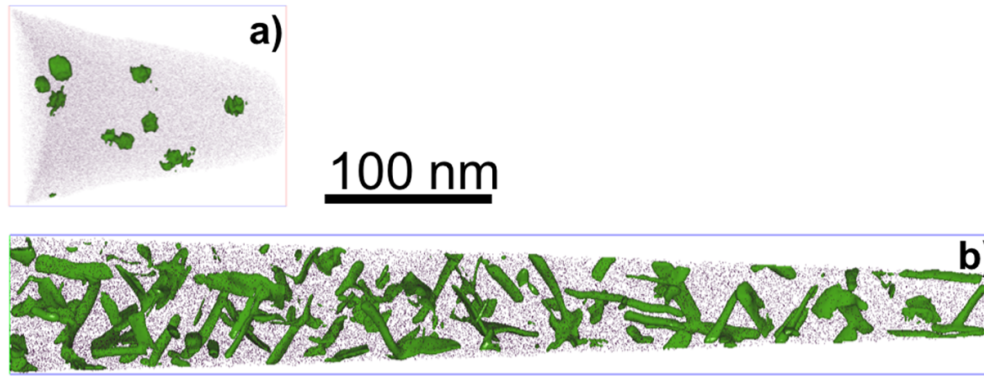
Figure 2. Atom maps showing the nucleation and maturation of the second phase precipitates in the single crystal irradiated tungsten for the 0.1 dpa case (*a*), and the 1.8 dpa (*b*). In both reconstructions, the points represent 1 % of all the W ions detected. Concentration isosurfaces are used to highlight the second phase precipitates, and these were constructed with (*a*) 1 at.% Re-Os, and (*b*) 12 at.% Re-Os.

Table 3. Precipitate chemistry in at.% for the low dose and high dose specimens. The bulk compositions (matrix and precipitate) determined by APT and from the FISPACT-II calculations are also included. The error given in the precipitate average values is the standard error of the mean. The minimum and maximum values are those from all the precipitates analysed.

| | 0.1 dpa | | | 1.8 dpa | | |
	W	Re	Os	W	Re	Os
Simulation (FISPACT-II)	98.21	1.66	0.10	82.37	8.59	8.99
Bulk (APT)	98.32	1.63	0.05	90.33	6.38	3.23
Precipitate (ave)	88.04±0.09	11.25±0.83	0.70±0.08	67.29±0.77	19.62±0.41	13.03±0.46
Precipitate (min)	82.71	8.52	0.48	55.44	14.13	6.31
Precipitate (max)	90.98	16.08	1.20	77.13	28.53	18.64

are shown in table 3, and in the ternary diagrams shown in figure 5.

For the low dose specimen, it can be seen that the bulk compositions for the experimentally obtained data and the FISPACT-II calculations match reasonably well, and that some Re has been produced, along with some Os. This is understandable in the low dose limit because Os is created from Re and so significant Re must be produced before quantifiable transmutation to Os can occur [17]. It is clear, however, that the spherical features shown in figure 2(*a*) are already showing signs of significant clustering of Re and Os above the matrix levels.

For the high dose specimen, there is a disparity between the predicted FISPACT-II results, and the bulk concentrations derived from the experimental data using the FISPACT-II information. This is more significant for the Os concentrations than for the Re. One reason for this discrepancy could be the effect of self-shielding [18]. While computational corrections for self-shielding were approximated in the FISPACT-II calculations (see [12] for details), the transport simulations used to evaluate the neutron irradiation field may miss the effect that self-shielding can have on the energy spectrum of neutrons seen by the samples—it was previously discussed in [18] how necessary it is to accurately predict the lower-energy components of neutron fields if simulations are to agree with experiment. In the case of the present experiments, there is uncertainty in the environment of the APT needles, whose position

within the irradiation capsule relative to the rest of the irradiated tungsten is not known (and thus not accounted for in the neutron transport simulations). The APT analysis could have been performed on W that has experienced significant self-shielding from surrounding W—such W would have received significantly lower neutron fluxes in the critical epithermal energies associated with the giant capture resonances (that cause self-shielding [2] and thus experience lower transmutation rates than predicted via simulations with the material-averaged neutron spectrum (both from W to Re and from Re to Os). However, this might not be the only cause of the discrepancy between simulation and experiment, nor may it be the dominant factor.

In [18] it was discussed how the local neutron environment, independent of self-shielding, can have a more dramatic impact on transmutation in W. In the present experiments, there is uncertainty in the wider experimental set-up, particularly concerning the local material environment surrounding the sample (and its variation in time), which could strongly influence the thermal neutron fluxes (i.e. because the mean free path of neutrons is relatively short at lower energies). For example, an approximate FISPACT-II calculation for the high dose case with the thermal component (energies below 0.5 eV) of the HFIR spectrum reduced to 25% of that used in the primary calculations shown in table 3, resulted in Re/Os concentrations of 6/4% – much closer to the experimental values. Such a difference in the actual neutron
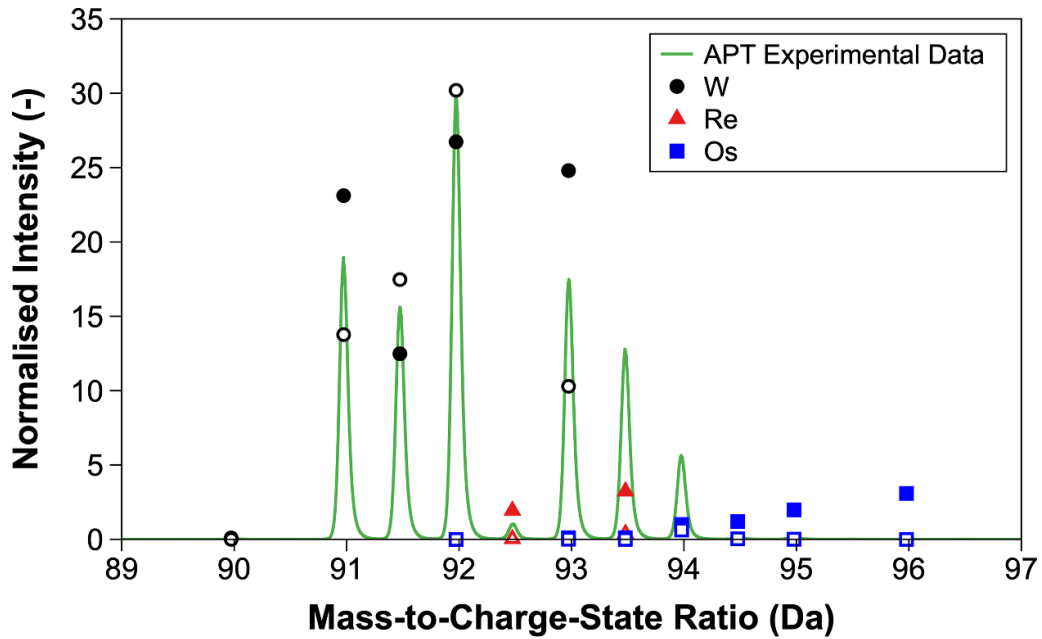
Figure 3. Mass-to-charge-state spectrum of the high-dose specimen in the range of the doubly charge ion state. The continuous green line shows the background corrected atom probe collected data. The colored points represent the natural abundances of the three main elements within the analyzed volume: W, Re, and Os. Open points represent the low dose case; closed point are the high dose case. The natural abundances do not correspond well with the peaks due to the generation and burn-up of different isotopes from the neutron irradiation and cooling.
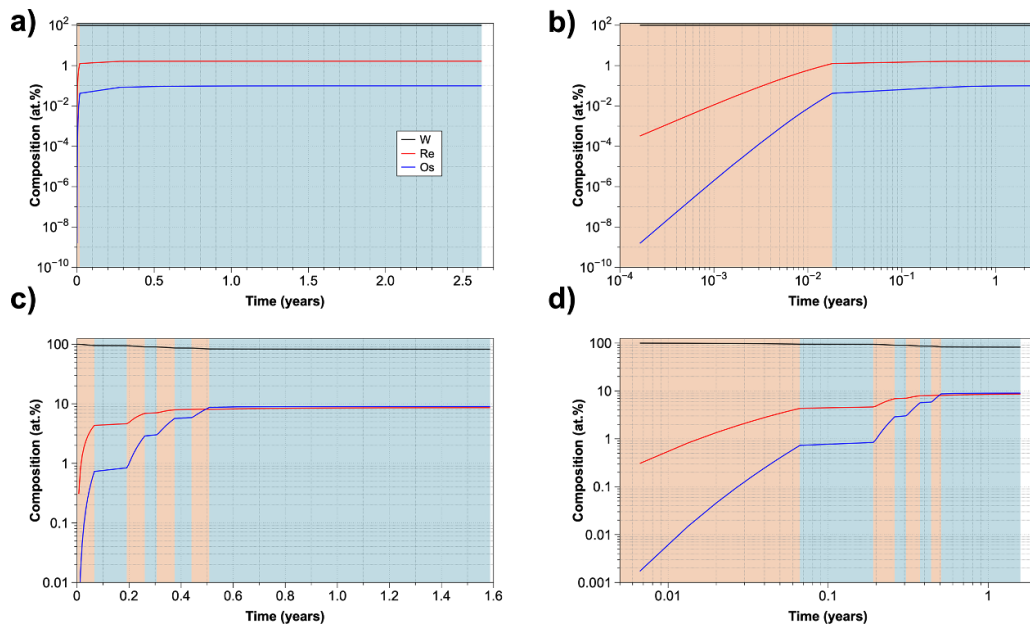

Figure 4. Summary of detailed inventory calculation results. Results from the FISPACT-II inventory calculations for the (*a*) and (*b*) low dose irradiation; (*c*) and (*d*) the high dose irradiation shown in both log-linear and log-log profiles for clarity. In both cases only the W, Re, and Os elements are shown as these are the initial product (W) primary transmutation products (Re and Os) under the primarily thermal neutron spectrum in HFIR. The graphs shows the growth in Re and Os under irradiation (the variation during decay-cooling during reactor cycles and before data collection is minor). The final elemental concentrations from these calculations were used as the abundances when performing peak deconvolution of the atom probe data.

spectrum experienced by the samples compared to the one provided is entirely possible if some unaccounted for, highly neutron-absorbing material were located close to the tungsten during the irradiation. Such a situation has previously been attributed to discrepancies between FISPACT-II simulations

and measurements on tungsten [18], which was resolved by properly accounting for additional materials surrounding the samples under investigation. It should be noted that this is difficult to quantify in the HFIR due to the highly transient nature of materials irradiation experiments in the HTF.
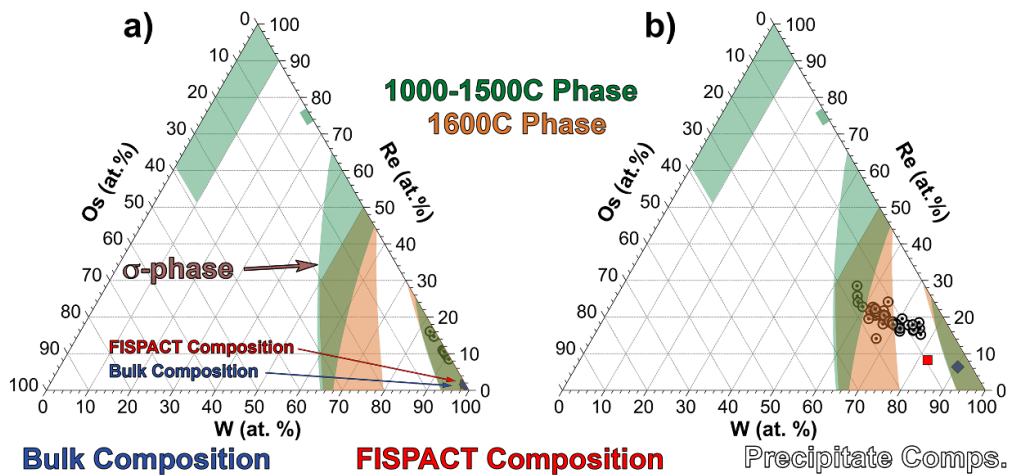
Figure 5. Ternary phase diagrams for the low dose specimen (*a*), and high dose specimen (*b*). The precipitate compositions are shown as black circles, the bulk compositions (including precipitates) are blue diamonds, and the bulk composition predicted by FISPACT inventory calculations is shown as a red square. Overlaid on the diagrams are the calculated phases for the W-Re-Os system.

Regardless of the discrepancy between the experiment and simulations, it is clear from table 3 and figure 2(*b*) that significant Re and Os is contained within the precipitates—the concentrations of Re/Os in the precipitates are significantly higher than in the bulk average.

In examining the composition of the precipitates to help in determining the phase, the compositions of individual precipitates/clusters has been plotted onto the ternary diagram shown in figure 5 along with the calculated phases for the temperatures 1000–1500 and 1600 °C . For the low dose case (figure 5(*a*) the composition of the clusters is observed to lie along (or very close to) the Re axis indicating that the clusters are predominantly Re-rich with little Os. This is consistent with the data presented in table 3, and with the expected transmutation where Re is produced and then Os (from the Re). At this stage, the clusters are not fully formed precipitates, but rather clusters enriched in Re.

The high dose precipitate compositions (figure 5(*b*) have shifted from the Re compositional axis further into the centre of the phase diagram due to the transmutation of Re into Os. Here it can be seen that the compositions are tending toward lying on a large shaded region of the plot that indicates the σ-phase region for the W-Re-Os phase diagram. Whilst there has been considerable discussion in the literature as to whether the precipitates are either σ- or χ-phase, the results here suggest that it is highly unlikely that the χ phase precipitates will be present from a compositional standpoint. It is also worth noting that the expected evaporation fields for Re (45) and Os (48) are lower than that of W (52) [19, 20] resulting in trajectory aberrations to occur that lead to higher atomic densities in the locale of the precipitates [21, 22]. The overall precipitate compositions are likely to be slightly underestimated and that the average composition of the precipitate will be pushed further into the σ-phase boundary.

Evidence of the effect of trajectory aberrations is also observed in the detector hit maps shown in figure 6; however, more work is required to fully elucidate the effect of

these trajectory aberrations on the precipitate compositions in neutron-irradiated tungsten specimens. Although there have been suggestions to correct this based on the change in point density [23], due to the significant overlap of isotopes generated due to the neutron irradiation and decay-cooling, this would be heavily complicated as a result of the significant non-natural abundances that this approach is not possible.

3.2. Cluster and precipitate formation and morphology

In the low dose case, the clusters formed have an approximately spherical morphology with a composition approximately that of W-1.7Re-0.1Os, (at.%) and with an approximate radius of 5 nm. This is commensurate with the results obtained previously on a series of W-2Re and W-1Re-1Os alloys self-ion irradiated up to 33 dpa at temperatures of 573 and 773 K [8]. At this point, it is worth noting that the clusters in the ion irradiated cases [8, 9] were both characterised using the maximum separation method for cluster analysis [24] whereas in the case presented here, the clusters have been characterised using the method of defining the clusters using composition isosurfaces, followed by a manual peak deconvolution method that will lead to differences in the cluster radii and compositions meaning that a quantitative comparison of the cluster sizes is not possible. The approach presented here has been used because of the non-natural abundances present in the material as a result of neutron-induced transmutation meaning that analysis using the maximum separation is not possible.

In the ion irradiated work [8], it was found that the Os preferentially clusters when compared to the Re, and that the inclusion of Os suppressed cluster growth. In the present case, the Re and Os concentrations are dynamic but at the snapshot in time during which they were examined there is insignificant Os and so relatively large clusters have formed.

Comparing the ion irradiated data [8, 9] to the low dose neutron irradiated samples, it is clear that the morphology is very similar despite the extremely large difference in damage
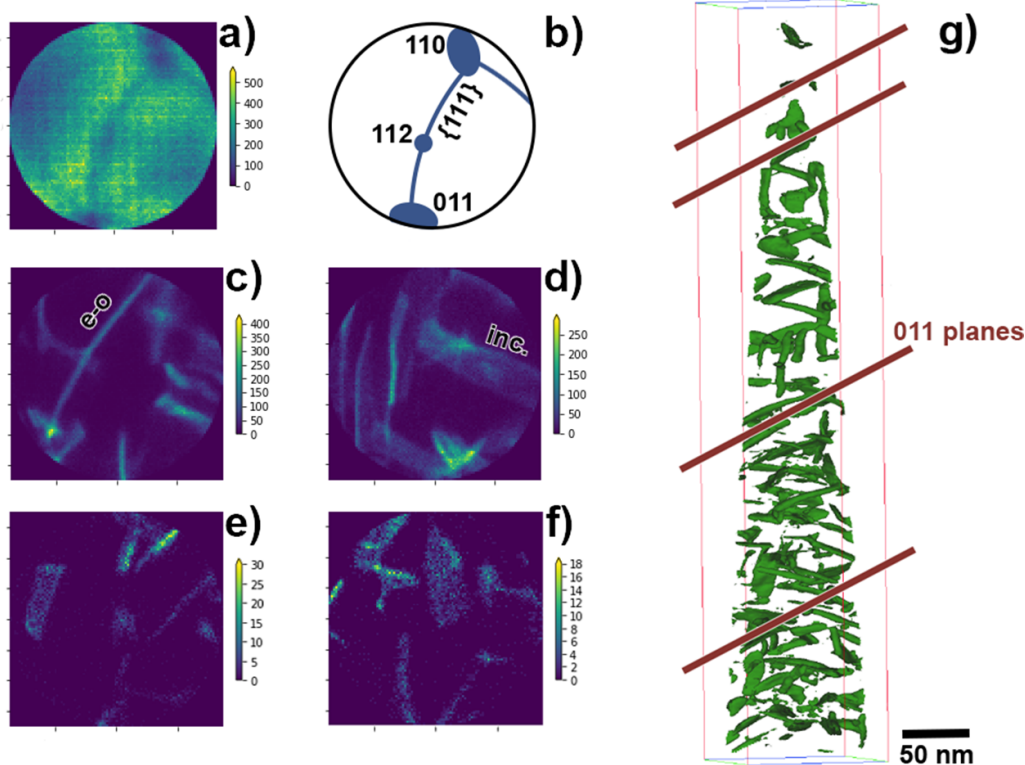
Figure 6. Filtered detector hit maps of the high dose sample showing the relationship between precipitates and matrix. (*a*) The detector hit map for the matrix showing the existence of 110 poles, and the 111 plane, (*b*) a schematic of the crystallography shown in (*a*), (*c*) and (*d*) reveal the presence of edge on (e–o) and incline (inc.) precipitates within the matrix in a detector hit map for the primary solutes Re and Os; (*e*) and (*f*) show the precipitates when the detector hit map is filtered to show only the data from the APT mass spectrum peak located at 62.67 Da corresponding to an isotope of transmutation products containing both Re and Os. An APT reconstruction showing a 12 at.% Re-Os isocomposition surface is shown in (*g*). The reconstruction was performed with the *z*-axis align along the 112 axis, and a significant number of precipitates are observed to lie along the 011 planes.

levels – 33 dpa compared to 0.1 dpa—yet similar Re concentrations. This demonstrably shows that the local concentration of solute dominates the resultant cluster morphology rather than the displacement damage level. While it could be argued that the increase in point defects may alter the nucleation and growth kinetics of the precipitates, here there is a two-orders of magnitude difference in irradiation dose (0.1 dpa compared to 33 dpa) and the difference in cluster size is negligible for the measurement methods used clearly demonstrating that the local solute concentration dominates the formation of clusters.

For the high dose samples shown in figure 2(*b*), it can be seen that the precipitates have formed with a rod- and ribbon-like morphology. By using an elemental filter of the detector hit maps of the atom probe data, it is possible to isolate the detector hit map of the precipitates to that of the host matrix. Some results of this analysis are shown in figure 6. Here, the detector hit map for the matrix is shown in figure 6(*a*), with a cartoon representation of the data in figure 6(*b*). The low index 110-type poles are visible, along with a higher order 112-type pole; a 111 plane is also visible. The detector hit maps shown in figures 6(*c*) and (*d*) show data that has been filtered to the solutes Re and Os and shows the presence of edge-on (*e-o*) and inclined (inc.) precipitates in the material. Another series of detector hit maps are shown in figures 6(*e*) and (*f*) in which case these detector hit maps have been filtered specifically to

the peak at a mass-to-charge-state ratio of 62.67 Da that corresponds to the $^{188}Re^{3+}$ and $^{188}Os^{3+}$ isotopes and shows the presence of edge-on and inclined precipitates. These specific isotopes were not present in the unirradiated material. The crystallographic relationship between the matrix and the precipitates is also confirmed by inspection of the planes in the APT reconstruction as shown in figure 6(*g*).

It is well understood that during the irradiation process in tungsten, the collision cascade collapses and dislocation loops are formed at the centre of the cascade [5–7]. Furthermore, depending on the alloy composition and irradiation temperature, dislocations with different habit planes and Burgers vectors can be formed, e.g. $\frac{1}{2}\langle 111 \rangle$ and $\langle 100 \rangle$. The precipitates shown in figure 6 appear to both have habit planes that are commensurate with dislocations having Burgers vectors $\frac{1}{2}\langle 111 \rangle$ and $\langle 100 \rangle$. It should also be noted that the number density of the precipitates is much higher than that typically observed in transmission electron microscopy (TEM) studies, e.g. [25]. This may be because the precipitates are lying along specific crystallographic habit planes and as such do not show in TEM images in all diffraction conditions.

Given that the Re and Os solutes are known to diffuse and trap at dislocations, it is proposed here that during the dynamic conditions of a neutron irradiation in which the composition and local microstructure is continuously evolving

(transmutation products forming, dislocation structures being produced and evolving) clusters are initially formed at the core of the dislocations, and that the precipitates tend to lie along the habit planes of the dislocations. Precipitates may then undergo further growth through trapping of transmutation products diffusing through the matrix, or by sequential collision cascades collapsing in the approximately same volume. Similar observations have been made in reactor pressure vessel steels in which Cu-rich precipitates form on dislocations based on an accumulation of solute concentration due to interactions between the solute atoms and radiation induced point defects. [26] Due to the highly dynamic nature of the system, the distribution of habit planes upon which the precipitates lie is not equivalent to the habit planes on which dislocations are for ion irradiation studies on model alloy systems, e.g. W-Re, W-Re-Os. The notion that the precipitates form on dislocations, and then evolve to lie along the initial habit plane on the dislocations within which they form is supported by the observation of the approximate angles subtended between the observed dislocations.

4. Conclusions

Characterisation of non-equilibrium second phase precipitates formed in single crystal tungsten under neutron irradiation up to damage levels of 1.8 dpa at approximately 700 °C   has been conducted using a combination of atom probe tomography and neutron inventory calculations in order to capture and understand their nucleation and formation, growth, and composition.

- In both doses, the transmutation resulted in changes in the elemental abundances that had to be accounted for in the APT analysis.
- At low dose, nanoscale spherical clusters rich in Re were formed. Compared to ion irradiation studies on model W-Re and W-Re-Os alloys, the cluster sizes are empirically larger. This observation fits with the previous conclusion that Os refines the size of the clusters.
- However, in contrast to the previous ion irradiation studies, formation of the Re-rich clusters appears to be dominated by the thermodynamics of the system with the contribution of radiation damage on the formation mechanisms being a minor component.
- Elemental analysis of the high dose material using inventory calculation informed decomposition of the mass spectrum revealed that the needle-like precipitate composition tended towards that of the σ-phase for the irradiation conditions used.
- The bulk and precipitate compositions were slightly different to that calculated by the inventory calculations by $\sim$2 at.% for Re and $\sim$5 at.% for Os in the high dose case, and this is attributed to a reduction in the thermal component of the neutron spectrum.
- The FISPACT-II calculations are informative in the determination of the compositions by serving as a guide to the peak fitting as they contain a significantly improved isotopic abundance ratios when compared to the natural abundances, particularly for the transmutation elements.
- The crystallographic relationship between the second phase precipitates and matrix was determined using APT methods. The results showed that the precipitates lie along habit planes similar to that of the dislocations—$\frac{1}{2}\langle 111\rangle$ and $\langle 100\rangle$, suggesting that irradiation induced dislocation loops serve as the primary nucleation and growth sites for the precipitates.
- A methodology for using inventory calculations combined with atom probe tomography has been demonstrated to evaluate precipitates in materials that suffer from significant transmutation under neutron irradiation, thereby enabling a better understanding of local chemistry of the precipitates.

The results of this study allows for a better understanding of the neutron irradiation induced precipitation in pure tungsten, and will enable the development of better atomistic and mechanistic models for the understanding and determination of the effects of radiation damage on physical properties in tungsten.

Notice

ORCID iDs

Philip D. Edmondson https://orcid.org/0000-0001-8990-0870
Baptiste Gault https://orcid.org/0000-0002-4934-0458
Mark R Gilbert https://orcid.org/0000-0001-8935-1744

References

[1] Armstrong D.E.J., Edmondson P.D. and Roberts S.G. 2013 Effects of sequential tungsten and helium ion implantation on nano-indentation hardness of tungsten *Appl. Phys. Lett.* **102** 251901

[2] Gilbert M.R. and Sublet J.-C. 2011 Neutron-induced transmutation effects in W and W-alloys in a fusion environment *Nucl. Fusion* **51** 043005

[3] Cottrell G.A., Pampin R. and Taylor N.P. 2006 Transmutation and phase stability of tungsten armor in fusion power plants *Fusion Sci. Technol.* **50** 89–98

[4] Ferroni F., Yi X., Arakawa K., Fitzgerald S.P., Edmondson P.D. and Roberts S.G. 2015 High temperature annealing of ion irradiated tungsten *Acta Mater.* **90** 380–93

[5] Yi X., Jenkins M.L., Briceno M., Roberts S.G., Zhou Z. and Kirk M.A. 2013 In situ study of self-ion irradiation damage in W and W–5Re at 500 °C *Phil. Mag.* **93** 1715–38

[6] Yi X., Jenkins M.L., Hattar K., Edmondson P.D. and Roberts S.G. 2015 Characterisation of radiation damage in W and W-based alloys from 2 MeV self-ion near-bulk implantations *Acta Mater.* **92** 163–77

[7] Mason D.R., Yi X., Kirk M.A. and Dudarev S.L. 2014 Elastic trapping of dislocation loops in cascades in ion-irradiated tungsten foils *J. Phys.: Condens. Matter.* **26** 375701

[8] Xu A., Beck C., Armstrong D.E.J., Rajan K., Smith G.D.W., Bagot P.A.J. and Roberts S.G. 2015 Ion-irradiation-induced clustering in W-Re and W-Re-Os alloys: A comparative study using atom probe tomography and nanoindentation measurements *Acta Mater.* **87** 121–7

[9] Xu A., Armstrong D.E.J., Beck C., Moody M.P., Smith G.D., Bagot P.A. and Roberts S.G. 2017 Ion-irradiation induced clustering in W-Re-Ta, W-Re and W-Ta alloys: An atom probe tomography and nanoindentation study *Acta Mater.* **124** 71–8

[10] Tanno T., Hasegawa A., Fujiwara M., He J.C., Nogami S., Satou M., Shishido T. and Abe K. 2008 Precipitation of Solid Transmutation Elements in Irradiated Tungsten Alloys *Mater. Trans.* **49** 2259–64

[11] Campbell A.A., Porter W.D., Katoh Y. and Snead L.L. 2016 Method for analyzing passive silicon carbide thermometry with a continuous dilatometer to determine irradiation temperature *Nucl. Instrum. Methods Phys. Res.* B **370** 49–58

[12] Sublet J.C., Eastwood J.W., Morgan J.G., Gilbert M.R., Fleming M. and Arter W. 2017 FISPACT-II: An Advanced Simulation System for Activation, Transmutation and Material Modelling *Nucl. Data Sheets* **139** 77–137

[13] Koning A.J., Rochman D. 2017 TENDL-2017 (https://tendl.web.psi.ch/tendl_2017/tendl2017.html)

[14] Miller M.K. and Russell K.F. 2007 Atom probe specimen preparation with a dual beam SEM/FIB miller *Ultramicroscopy* **107** 761–6

[15] Gault B., Haley D., de Geuser F., Moody M.P., Marquis E.A., Larson D.J. and Geiser B.P. 2011 Advances in the reconstruction of atom probe tomography data *Ultramicroscopy* **111** 448–57

[16] Larson D.J., Prosa T.J., Ulfig R.M., Geiser B.P. and Thomas F.K. 2013 *Ultramicroscopy Local Electrode Atom Probe Tomography: a Users Guide* (New York: Springer)

[17] Greenwood L. and Garner F. 1994 Transmutation of Mo, Re, W, Hf and V in various irradiation test facilities and STARFIRE *J. Nucl. Mater.* **212-215** 635–9

[18] Gilbert M.R., Sublet J.-C. and Dudarev S.L. 2017 Spatial heterogeneity of tungsten transmutation in a fusion device *Nucl. Fus.* **57** 044002

[19] Gault B., Moody M.P., Cairney J.M. and Ringer S.P. 2012 *Atom Probe Microscopy* (New York: Springer)

[20] Dagan M., Hanna L.R., Xu A., Roberts S.G., Smith G.D.W., Gault B., Edmondson P.D., Bagot P.A.J. and Moody M.P. 2015 Imaging of radiation damage using complementary field ion microscopy and atom probe tomography *Ultramicroscopy* **159** 387–94

[21] Bachhav M.N., Odette G.R. and Marquis E.A. 2014 Alpha-prime precipitation in neutron-irradiated Fe-Cr alloys *Scr. Mater.* **74** 48–51

[22] Edmondson P., Parish C. and Nanstad R. 2017 Using complimentary microscopy methods to examine Ni-Mn-Si-precipitates in highly-irradiated reactor pressure vessel steels *Acta Mater.* **134** 31–9

[23] Blavette D., Vurpillot F., Pareige P. and Menand A. 2001 A model accounting for spatial overlaps in 3D atom-probe microscopy *Ultramicroscopy* **89** 145–53

[24] Hyde J.M., Marquis E.A., Wilford K.B. and Williams T.J. 2011 A sensitivity analysis of the maximum separation method for the characterisation of solute clusters *Ultramicroscopy* **111** 440–7

[25] Katoh Y. *et al* 2019 Response of unalloyed tungsten to mixed spectrum neutrons *J. Nucl. Mater.* **520** 193–207

[26] Smith G.D.W., Hudson D., Styman P.D. and Williams C.A. 2013 Studies of dislocations by field ion microscopy and atom probe tomography *Phil. Mag.* **93** 3726–40